

Functional Brain Mapping & Analysis

Ahmed Mohamed Ali^{#1}, Osama Mohamed Ali^{#2}

Systems and Biomedical Engineering Department, Cairo University

* Neuroscience

Abstract— The human brain is composed of distinct regions that are responsible for various cognitive functions, sensory processing, and motor control. Understanding the complex relationship between these regions and their roles in activities such as movement, language, and memory is crucial for advancing brain research. This paper presents a detailed analysis of brain modeling techniques, with a focus on functional magnetic resonance imaging (fMRI) to map neural activity. By utilizing fMRI, we are able to visualize brain regions activated during specific tasks, offering insights into the brain's functional organization. Our study demonstrates how task-specific brain activity, such as motor movement or cognitive processing, correlates with the activation of distinct regions, providing a foundation for future investigations into neural connectivity and brain function.

I. INTRODUCTION

Functional magnetic resonance imaging (fMRI) has emerged as a leading neuroimaging technique that enables researchers to investigate the intricate workings of the human brain in real time. By measuring changes in blood flow, fMRI provides insights into neural activity, revealing which brain regions are engaged during specific cognitive and motor tasks. This technique relies on the principle that active neurons consume more oxygen, leading to a localized increase in cerebral blood flow. This hemodynamic response is captured by fMRI as a Blood Oxygen Level Dependent (BOLD) signal, which serves as an indirect marker of neural activity.

The Flanker task, utilized in this study, is a well-established cognitive paradigm that assesses attention and cognitive control. Participants are presented with a series of stimuli, such as arrows or other figures, and must respond based on the direction of a central target, often flanked by congruent or incongruent distractors. As illustrated in Figure 1, the task requires participants to make rapid decisions, allowing for the examination of how conflicting information impacts response time and accuracy. By utilizing the Flanker dataset, we can investigate the underlying brain mechanisms that contribute to these cognitive processes, particularly in distinguishing between congruent and incongruent conditions.

Our analysis will involve a multi-step approach, beginning with the critical task of preprocessing the fMRI data. This includes identifying and mitigating noise and motion artifacts, which can significantly affect the quality of the BOLD signal. We will conduct a thorough assessment of signal consistency to ensure the reliability of our findings. Following this preprocessing stage, we will employ FSL (FMRIB Software Library) to

conduct full-level analysis of the preprocessed data. FSL offers a robust suite of tools for analyzing fMRI data, allowing us to delineate active brain regions and their associated functions during the Flanker task.

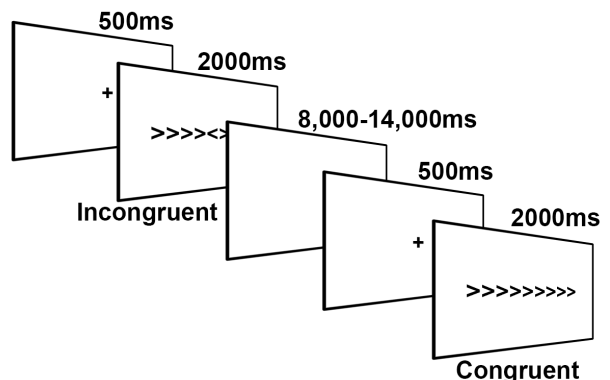


fig.(1) shows the Flanker task, where subjects first see a white screen, then a fixation cross ("+"), followed by an image. The image appears for 500 ms, 2,000 ms, then between 8,000 ms and 14,000 ms, prompting a response based on the image.

By examining brain activity in this context, our study aims to enhance our understanding of the neural correlates of cognitive control and attentional processes, shedding light on how different brain regions interact and contribute to behavioral outcomes. Ultimately, this research will provide valuable insights into the complexities of brain function, with implications for understanding various neurological and psychiatric conditions.

II. DATASET:

The "NYU Slow Flanker" dataset consists of data collected from 26 healthy adults engaged in a slow event-related Eriksen Flanker task. It is important to note that all data has been uploaded regardless of quality; therefore, users are responsible for assessing data quality, including potential movement artifacts and other issues.

During each trial, participants indicated the direction of a central arrow within an array of five arrows by pressing one of two buttons on a response pad. The inter-trial interval (ITI) varied between 8 to 14 seconds, with a mean ITI of 12 seconds. In congruent trials, the flanking arrows pointed in the same direction as the central arrow (e.g., <<<<<), whereas in incongruent trials, the flanking arrows pointed in the opposite direction (e.g., <<><<).

Participants completed two five-minute blocks, each containing 12 congruent and 12 incongruent trials presented in a pseudorandom order.

Functional imaging data were acquired using a research-dedicated Siemens Allegra 3.0 T scanner equipped with a standard Siemens head coil at the NYU Center for Brain Imaging. A total of 146 contiguous echo planar imaging (EPI) whole-brain functional volumes were obtained for each of the two Flanker task blocks, with the following parameters: repetition time (TR) of 2000 ms, echo time (TE) of 30 ms, flip angle of 80 degrees, 40 slices, a matrix size of 64x64, a field of view (FOV) of 192 mm, and an acquisition voxel size of 3x3x4 mm. Additionally, a high-resolution T1-weighted anatomical image was acquired using a magnetization-prepared gradient echo sequence (MPRAGE) with the following parameters: TR of 2500 ms, TE of 3.93 ms, inversion time (TI) of 900 ms, flip angle of 8 degrees, 176 slices, and an FOV of 256 mm.

III. METHODOLOGY

Before conducting the first-level analysis, we performed a critical preprocessing step involving brain extraction. This process is essential for isolating brain tissue from non-brain structures within the magnetic resonance imaging (MRI) data. To optimize brain extraction, we examined the effects of various fractional intensity thresholds by systematically adjusting these threshold values. This approach allows us to identify differences in the resulting brain masks and variations across different threshold levels.

Each fractional intensity threshold represents a unique method for delineating brain tissue from non-brain regions. Lower threshold values encompass a broader range of intensities, which may inadvertently include more non-brain tissue alongside the desired brain matter. Conversely, higher threshold values limit the inclusion of non-brain structures, potentially leading to a more refined extraction of the brain region.

Through this comparative analysis, we aim to elucidate the impact of threshold selection on the quality and extent of brain extraction. By evaluating the variations across different threshold values, we seek to determine the optimal threshold for our specific dataset and research objectives.

Threshold = 0.1

As illustrated in Figure 2, employing a low fractional intensity threshold (0.1) resulted in a suboptimal brain extraction outcome. The resultant brain mask exhibited significant inclusion of non-brain tissues, such as bone marrow and fragments of the skull. This suggests that the lower threshold value was ineffective in discriminating between brain and non-brain structures, leading to an incomplete extraction process.

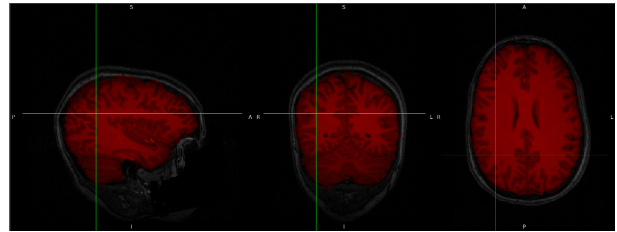


fig.(2)

Threshold = 0.9

In contrast, as depicted in Figure 3, the application of a high fractional intensity threshold (0.9) led to an extraction outcome where a substantial portion of the original brain tissue was absent. The resultant brain mask primarily consisted of a small fraction of the actual brain tissues, indicating that the higher threshold value resulted in an overly conservative extraction process.

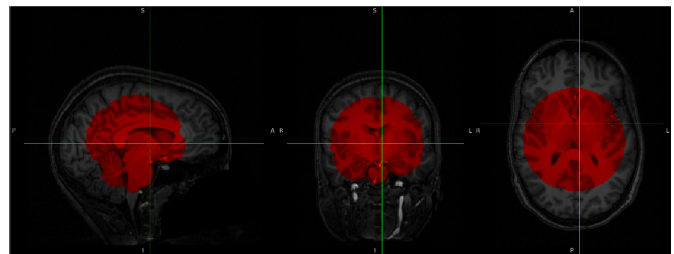


fig.(3)

In conclusion, the selection of fractional intensity threshold during brain extraction requires careful consideration. While a high threshold may reduce the risk of including non-brain tissues, it also poses the danger of significant data loss, potentially excluding critical brain regions of interest.

Conversely, a lower threshold broadens the inclusion of brain tissues but risks incorporating non-brain structures.

Striking a balance between inclusivity and precision is paramount. Although a lower threshold may lead to the inclusion of unintended non-brain tissues, it ensures a comprehensive representation of brain regions, safeguarding against the inadvertent exclusion of vital areas, such as active regions of interest.

Ultimately, the optimal threshold selection depends on the specific characteristics of the MRI data and the objectives of the study. By carefully evaluating the trade-offs between inclusivity and precision, researchers can make informed decisions that enhance the fidelity and relevance of brain extraction outcomes in their analyses.

As shown in Figure 4, utilizing a fractional intensity threshold of 0.1 reveals that certain non-brain tissues are inadvertently incorporated into the extracted mask. This observation underscores the inherent challenge of balancing inclusivity with precision in brain extraction processes.

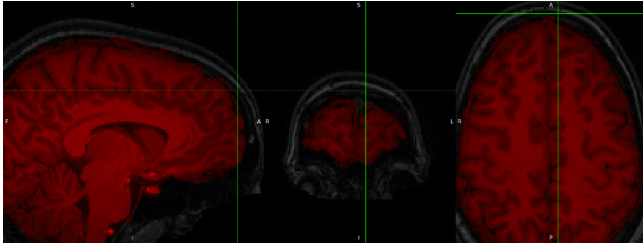


fig.(4)

First-Level Analysis Using FEAT

In our analysis, we utilized the FEAT (Functional MRI Expert Analysis Tool) graphical user interface (GUI) to perform first-level analysis on the neuroimaging data. Focusing on a single subject's run, we initiated the preprocessing phase by carefully configuring the necessary parameters to ensure robust data preparation.

During this preprocessing, we executed motion correction using MCFLIRT (Motion Correction FMRIB's Linear Image Registration Tool) to mitigate motion artifacts and enhance overall data quality. Given the relatively small repetition time (TR) of 2000 ms, we determined that slice timing correction was unnecessary for this dataset, thereby streamlining the preprocessing workflow. Additionally, we selected a smoothing kernel of 5 mm to facilitate spatial smoothing, which promotes noise reduction and enhances statistical sensitivity during subsequent analysis stages.

The preprocessing also involved registering subject-specific structural images to the MNI (Montreal Neurological Institute) space, designating the MNI152 2mm template as the target for alignment. To ensure accurate registration, we employed a normal search for reference voxels, which allowed for a comprehensive exploration of the spatial correspondence between the subject images and the MNI template. Furthermore, we specified a 12 degrees-of-freedom (DOF) affine transformation to accommodate potential variations in global scaling, rotation, and translation between the two spaces.

Results of Preprocessing

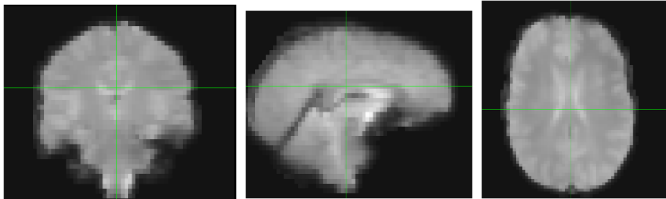


Figure 5 illustrates the mapping of high-resolution subject-specific images to standard space, a critical step that transforms individual subject images into a standardized anatomical reference space, thereby facilitating cross-subject comparisons. Figure 6 showcases the outcome of mapping functional neuroimaging data to standard space, enabling the alignment of functional activation patterns across different subjects onto a common anatomical framework, which is essential for group-level analyses and enhances the interpretability of findings.

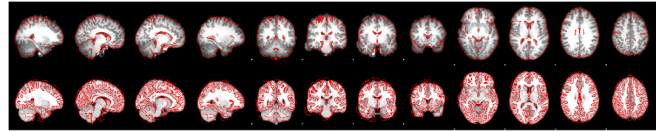


fig.(5)

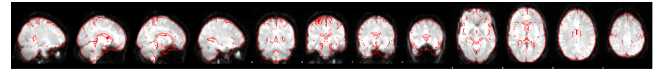


fig.(6)

Motion Correction Analysis

Figure 7 presents the results of the motion analysis, revealing significant translational motion along the z-axis, exceeding 2 mm. This displacement surpasses the dimensions of a single voxel in the MNI standard space, raising concerns regarding potential confounding effects on data integrity and interpretation. In Figure 8, the analysis highlights the presence of rotational motion, with the most significant rotation observed in the y-direction, measuring 0.005 radians. This parameter provides insights into the stability of the imaging acquisition process and assists in evaluating potential sources of variability within the dataset. Additionally, Figure 9 shows the analysis of mean displacement, indicating a maximum relative movement of 0.213 millimeters, while the absolute maximum recorded was 0.32 millimeters. This metric offers a comprehensive assessment of the overall motion observed within the dataset, furnishing critical insights into the extent of subject movement throughout the imaging session.

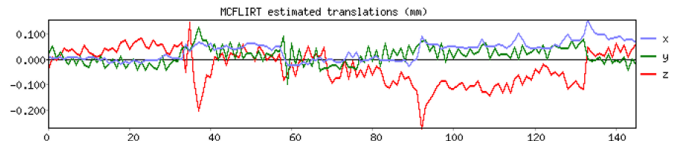


fig.(7)

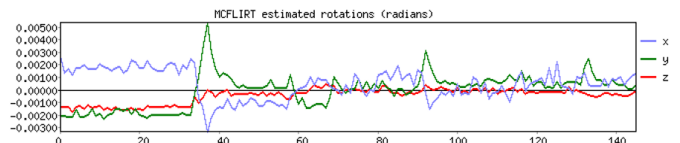


fig.(8)

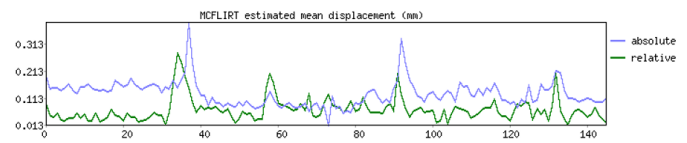


fig.(9)

Smoothing Analysis

The choice of smoothing kernel significantly influences the outcome of the analysis. When employing a smoothing kernel of 12 mm, as illustrated in Figure 10, the image exhibits a notably blurred appearance, resulting in minimal discernible anatomical structures. This extensive smoothing operation effectively reduces noise but compromises the structural integrity and clarity of the image. Conversely, Figure 11 demonstrates the application of a 3 mm smoothing kernel, which preserves finer anatomical details while still achieving reasonable noise

reduction. The smaller kernel size strikes a better balance between smoothing and structural preservation, enhancing the clarity and discernibility of anatomical features.

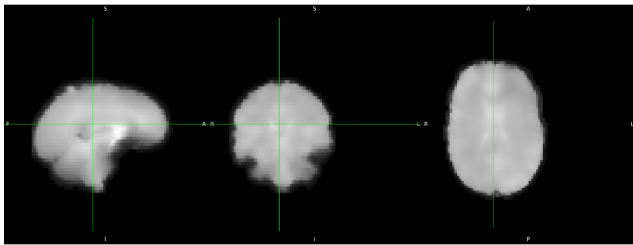


fig.(10)

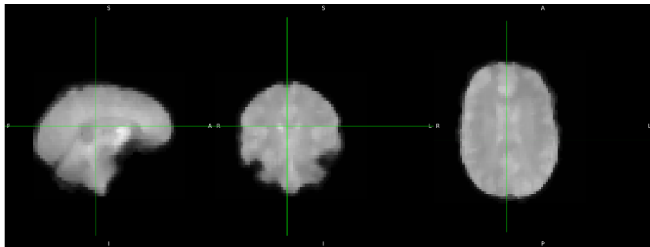


fig.(11)

Preprocessing with Degrees of Freedom

In Figure 12, we illustrate the mapping of functional data onto the high-resolution structural image utilizing a transformation with only 3 degrees of freedom, primarily focusing on translation. This limited transformation accounts solely for shifts in position, neglecting rotational or scaling adjustments. Figure 13 reveals that mapping functional data to standard space using only 3 degrees of freedom leads to noticeable discrepancies between the functional data and the standard template. The restricted motion parameters fail to adequately capture the intricate spatial variability inherent in the data, resulting in suboptimal alignment. In contrast, Figure 7 demonstrates that employing 12 degrees of freedom produces vastly improved alignment outcomes. By incorporating a broader spectrum of motion parameters, including translation, rotation, and scaling, the registration process adeptly captures the nuanced spatial variations present within the data.

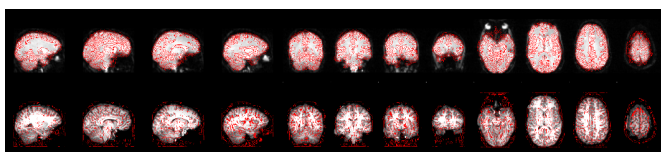


fig.(12)



fig.(13)

Boundary-Based Registration (BBR)

Figure 14 depicts the functional data mapped onto the high-resolution structural image registered using Boundary-Based Registration (BBR). Despite the increased processing time associated with this method, the resulting alignment does not exhibit noticeable differences discernible to the human eye compared to the alignment achieved with 12 degrees of freedom. This observation suggests that BBR

effectively captures the necessary spatial adjustments, leading to comparable alignment outcomes despite the longer processing duration.

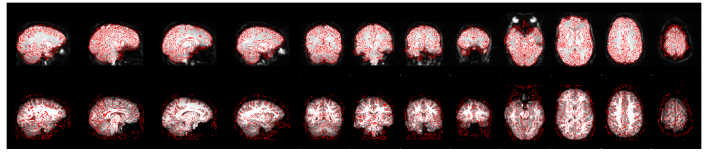


fig.(14)

Considerations for Choosing Registration Methods

When selecting between 12 degrees of freedom and BBR, it is crucial to consider the specific characteristics of the data. BBR is particularly advantageous when aligning functional data to high-resolution structural images, especially in situations where significant anatomical differences or distortions exist. By optimizing registration through focusing on tissue boundaries, BBR can improve accuracy in complex anatomical regions. On the other hand, utilizing 12 degrees of freedom is preferred when there are substantial differences in position, orientation, or scale between functional and structural images, providing greater flexibility to capture complex spatial transformations, albeit with increased computational complexity and processing time.

First level analysis

To facilitate the creation of a General Linear Model (GLM) in FSL, we first converted the content of TSV files into a format compatible with FSL. This step is crucial for analyzing the neuroimaging data associated with our task. The time series included two distinct regressors, representing incongruent and congruent events, which are characterized by their non-overlapping occurrences.

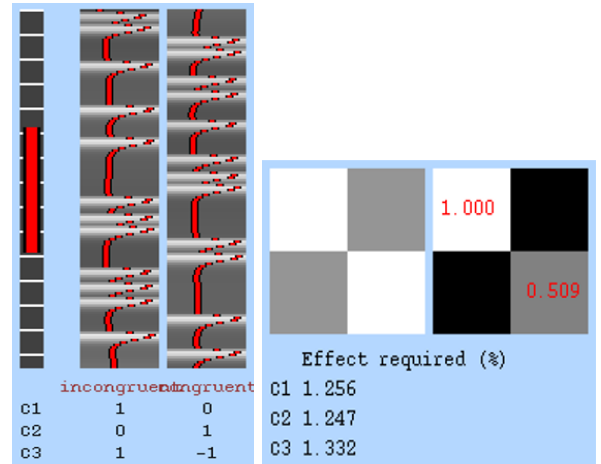


fig.(15) It depicts the time series for two regressors representing incongruent and congruent events for the first run of the first subject, illustrating that these events do not occur simultaneously.

In our analysis, we defined three contrasts to examine the effects of these conditions: the first contrast focused on the incongruent events, while the second highlighted the congruent events. The third contrast compared the two conditions directly, providing insights into the differences in brain activation associated with each task type.

We computed parameter estimates for the incongruent regressor, which was set to 1, while the congruent regressor was set to 0. This mapping revealed the active regions of the brain engaged

during incongruent tasks, allowing us to identify specific areas of interest. In Figure 16, This map highlights the active regions during this task, overlaid on the filtered brain, representing the z1 result. Similarly, we evaluated the active regions during congruent tasks by setting the congruent regressor to 1 and the incongruent regressor to 0, thereby isolating the regions specifically associated with congruent conditions.

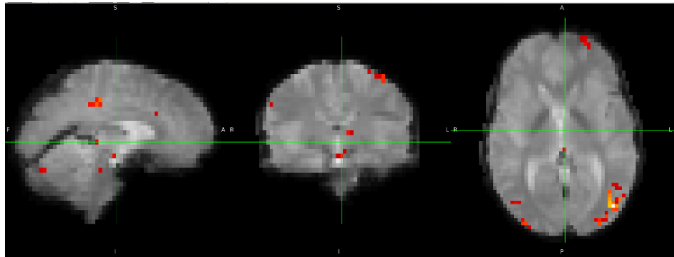


fig.(16)

Additionally, the contrast between incongruent and congruent conditions was assessed, with the incongruent regressor set to 1 and the congruent regressor to -1. This analysis highlighted the differences in activation patterns between the two conditions, providing a comprehensive understanding of how task demands influence brain activity.

Through this approach, we aimed to elucidate the neural mechanisms underlying cognitive processes associated with the Flanker task, contributing to our overall understanding of brain function during task execution.

2nd-Level-Analysis

The second-level analysis in this fMRI study involves averaging parameter and contrast estimates from the first-level analysis across all subjects. The goal is to extract group-level insights from the data. The first step in this process is to create FEAT directories for all 26 subjects, which involves applying the steps from the first-level GLM modeling for each individual. This includes specifying the subject's 4D fMRI data, conducting brain extraction (BET), creating explanatory variables (EVs) and contrast of parameter estimates (COPEs), and linking the appropriate timing files. Once these steps are completed, a design file is generated for each run of the experiment, resulting in two design files per subject, representing each experimental run (run1 and run2). To automate the processing for all subjects, a script is used to iterate over each subject's data, copying the design files, adjusting subject-specific parameters, and initiating FEAT analysis for both experimental runs. This ensures that the same process is applied consistently across all 26 subjects, generating a corresponding FEAT directory for each. Following this, the directories need to be renamed to maintain consistency in naming conventions. Initially, the directories are named according to the subject's identifier and task, which can vary depending on the subject and task. To facilitate further analysis, a renaming script is employed to standardize the names to 'run1' and 'run2' across all subjects. Once all FEAT directories are named consistently, the next step is to retrieve the full paths for all directories to prepare for the higher-level analysis. This step is critical because these paths are used as inputs for the

group-level analysis, ensuring that the software can correctly access the results from each subject's first-level analysis. The higher-level analysis is conducted using the FSL software, where the option for "higher-level analysis" is selected. The number of inputs is set to 52, corresponding to two runs for each of the 26 subjects. The paths to the FEAT directories, which were obtained in the previous step, are then input into the software. A "Fixed Effects" model is chosen to aggregate the results across subjects' runs, assuming that the effects observed are consistent across runs for each individual subject.

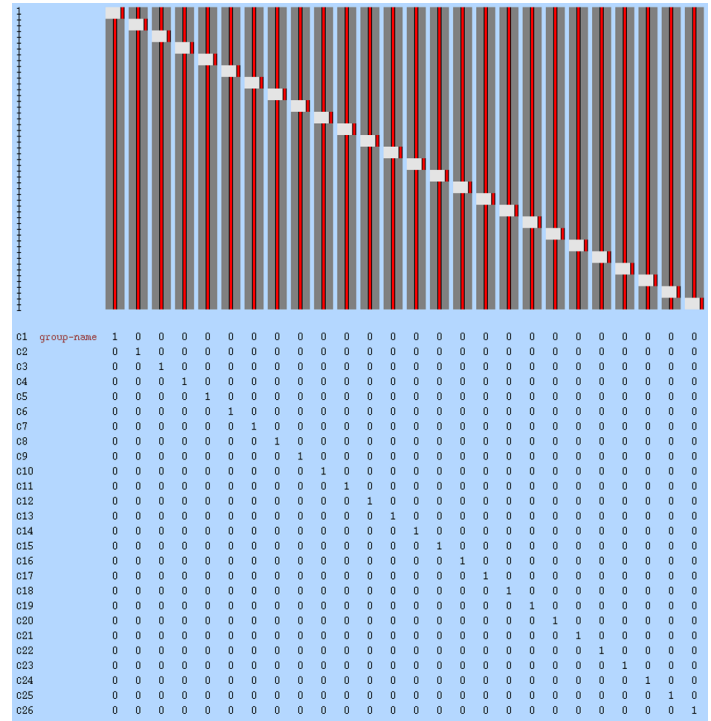


fig.(17) Final GLM design matrix for all 26 subjects averaging their runs.

After FSL completes the higher-level analysis, the output is a comprehensive HTML page that contains all relevant information from the 26 subjects involved in the study. This includes the input paths for each subject's run, alongside the FEAT directories and the associated registration images for each subject. The page also provides the transformed brain images from the individual subject space into the standard space, including a summation of the masks across all subjects. The result section features the design matrix along with external pages for each contrast of parameter estimates (COPE) specified in the lower-level analysis, which in this case, were for incongruent, congruent, and the difference between incongruent and congruent conditions. Each of these COPEs is accompanied by detailed z-statistics and time-series plots for all 26 subjects, allowing for a thorough review of the results. The FSL higher-level analysis streamlines the entire process, minimizing the potential for errors that could occur during manual extraction of BET, FEAT, and GLM models. By leveraging scripting to automate subject name handling and other repetitive tasks, this approach facilitates the analysis of large datasets with greater efficiency, reducing the likelihood of

errors while increasing the accuracy and reliability of the results. This automation not only speeds up the process but also enhances the quality of the analysis, leading to more precise findings and making the investigation of neural data easier and more effective.

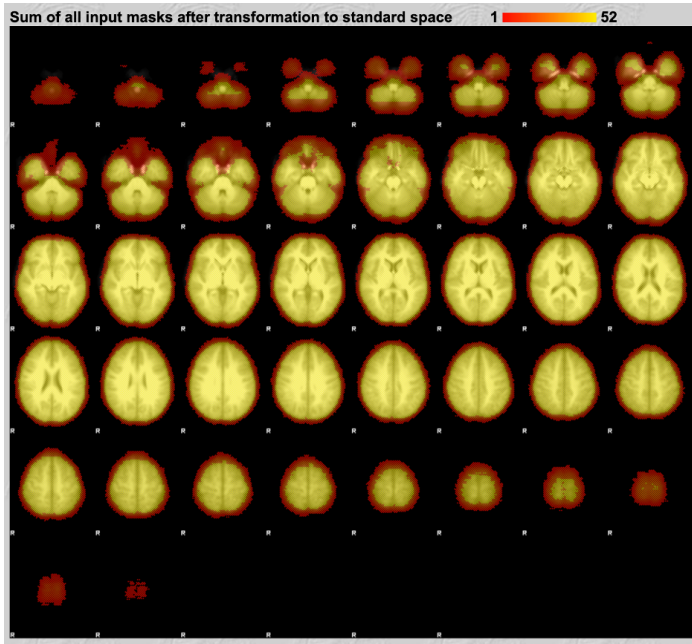


fig.(18)

3rd-Level-Analysis

Third-level analysis in fMRI is a critical step for enhancing the statistical power of studies by aggregating data across multiple subjects, which helps in identifying consistent patterns of brain activity at the group level. This level of analysis goes beyond individual variability, focusing on effects that are generalizable across participants, thus providing insights that are more reliable and valid. In cognitive neuroscience, clinical research, and psychological studies, third-level analysis is essential for understanding common neural mechanisms that are consistent across individuals, offering a more generalizable understanding of brain function. The process of third-level analysis begins with the extraction of COPE images, which represent the contrasts of parameter estimates from each subject's first- and second-level analyses. These images, typically located in the stats subfolder of each COPE folder, are gathered and organized for group-level analysis. Using FSL FEAT, researchers then configure a higher-level analysis, where the input is defined as 3D COPE images from all subjects. The number of inputs corresponds to the number of subjects being analyzed, and paths to these images are provided to the software. A key aspect of third-level analysis is the use of the General Linear Model (GLM) for mixed-effects modeling. Mixed-effects models are crucial because they account for both within-subject and between-subject variability, which is essential for ensuring that the results can be generalized beyond the specific sample being studied. FSL's FLAME 1 (FMRIB's Local Analysis of Mixed Effects) is commonly used to provide accurate parameter estimates by integrating this

variability. The model setup often involves defining a single-group average, where the data from all subjects are pooled to assess group-level effects. Following the setup of the GLM, thresholding techniques are applied in the post-stats phase to determine the statistical significance of the results. Several methods are available for thresholding, each with its own strengths and limitations. For example, no thresholding displays all statistical values without filtering for significance, providing a comprehensive view of the data but increasing the likelihood of including noise. Uncorrected thresholding, in contrast, applies a p-value threshold without correcting for multiple comparisons, which can detect strong signals but also increases the risk of false positives. More stringent methods, such as voxel-wise correction, adjust for multiple comparisons at the voxel level, reducing the likelihood of false positives but potentially missing subtle signals. Cluster-wise correction, on the other hand, focuses on identifying spatially extended clusters of activity, balancing sensitivity and specificity by emphasizing coherent patterns of activation across multiple voxels.

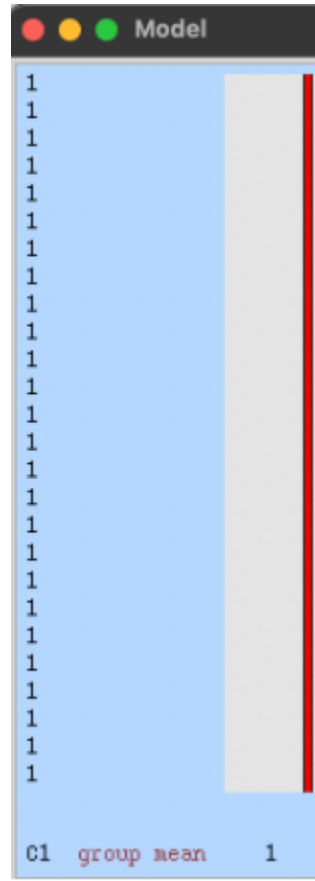


fig.(19)

The results of applying different thresholding techniques during third-level analysis revealed significant variations in the identification of brain activations across the three COPEs, highlighting the importance of selecting appropriate thresholding methods to ensure reliable fMRI data interpretation. When no thresholding was applied, no meaningful images were produced. This indicates that without a threshold to differentiate between brain signals, the results are dominated by noise, suggesting that thresholding is crucial for isolating meaningful

neural activations. For the uncorrected thresholding technique, the results for COPEs 1, 2, and 3 displayed large areas of brain activation. However, due to the lack of correction for multiple comparisons, these widespread activations may not accurately reflect true neural processes and are more likely to introduce errors in the analysis. In COPEs 1 and 2, significant activations were found in regions associated with cognitive control and error processing, while COPE 3, which examines differences between incongruent and congruent tasks, showed distinct activations highlighting the brain regions involved in task differentiation. Despite the detected activations, this method is prone to false positives, limiting its reliability for robust analysis.

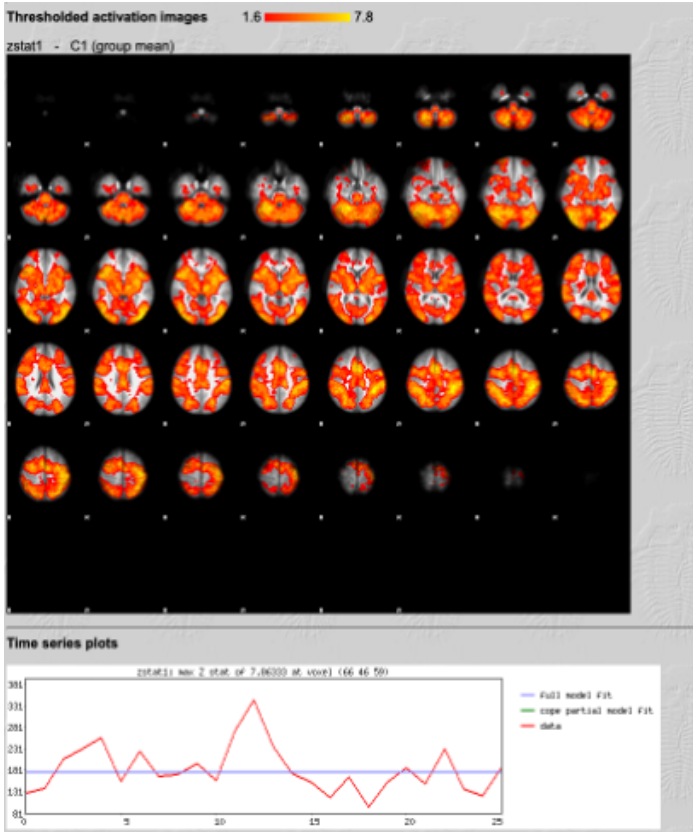


fig.(20) COPE 1 Results of uncorrected technique

With voxel-wise thresholding, the results became more refined. The activation maps for COPEs 1 and 2 showed statistically robust activations related to cognitive control and error processing, benefiting from the method's correction for multiple comparisons. This approach minimizes the risk of false positives while maintaining sensitivity to true neural responses. However, it reduced the size of activation regions, potentially overlooking subtle effects. This tradeoff was especially apparent in COPE 3, where the minimal difference between incongruent and congruent task activations led to no significant regions being detected.

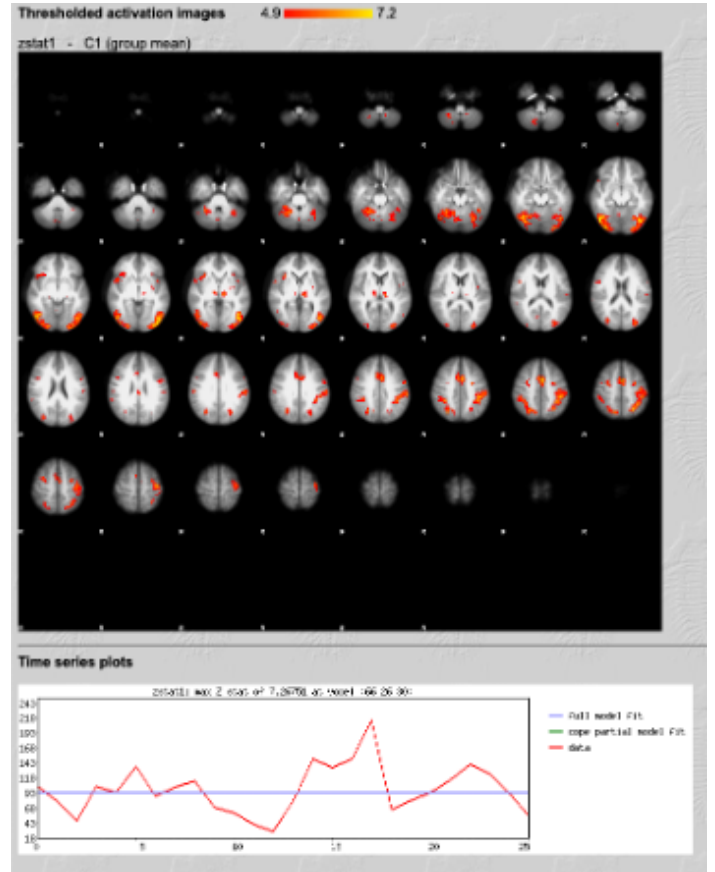


fig.(21) COPE 1 Results of voxel-wise technique

Cluster thresholding, on the other hand, provided a balance between sensitivity and specificity. By focusing on spatially extended patterns of activation and correcting for multiple comparisons at the cluster level, this technique identified robust neural activations across all COPEs. The results for COPEs 1 and 2 aligned well with known regions involved in cognitive control and error processing, while COPE 3 showed a clearer, though minimal, difference between incongruent and congruent task activations. This approach not only reduced false positives but also captured broader activation patterns, making it the most comprehensive method for this third-level analysis.

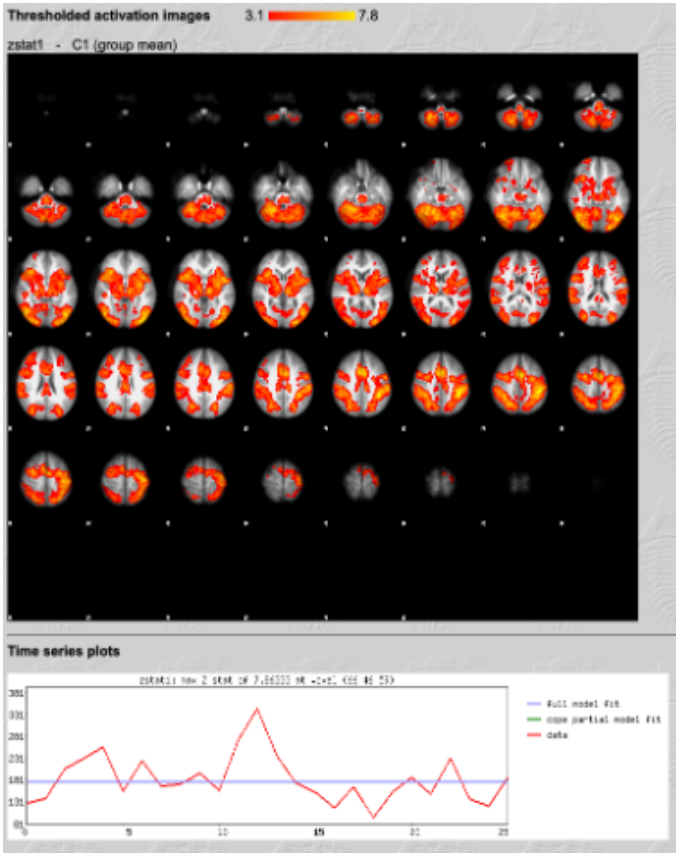


fig.(22) COPE 1 Results of cluster technique

Resulting regions

Upon visualizing the results in FSLEYES using voxel thresholding, it was evident that the primary brain regions activated during the incongruent task (COPE1) included the right and left cerebral cortex, as well as regions like the right putamen and the lateral occipital cortex. The cerebral cortex, known for its role in higher-order cognitive functions such as thinking, consciousness, and problem-solving, showed significant activation, which aligns with the cognitive demands of processing incongruent stimuli. The activation in the putamen is also notable, as this region is associated with motor control and learning, potentially reflecting the effort involved in managing conflicting information. Similarly, the lateral occipital cortex, which is involved in visual processing, might be engaged due to the visual nature of the flanker task. These patterns of activation suggest that the brain recruits areas responsible for complex cognitive tasks when handling incongruent signals, highlighting the intricate neural mechanisms underlying cognitive control and conflict resolution.



fig.(23) COPE 1 activated regions

The regions activated in COPE2 largely overlapped with those observed in COPE1, reflecting the cognitive similarities between the tasks. Significant activity was predominantly found in the right and left cerebral cortex, particularly in the lateral occipital cortex (both the inferior and interior divisions), along with notable activation in the cingulate gyrus. The lateral occipital cortex, involved in visual processing, likely contributes to the task's visual demands, while the cingulate gyrus is crucial for cognitive control and decision-making. This convergence of activation across these regions underscores their role in high-order cognitive functions, such as problem-solving and managing cognitive control, which are essential for handling both congruent and incongruent tasks. The overlap in activation patterns suggests that similar neural mechanisms are at play during both types of tasks, reflecting the brain's consistent engagement in processing complex cognitive challenges.

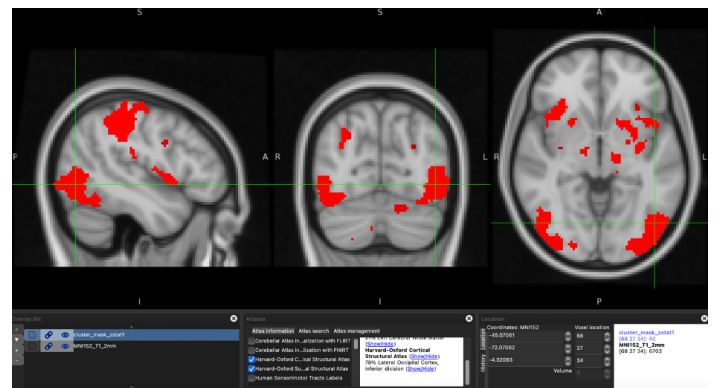


fig.(24) COPE 2 activated regions

The difference between the incongruent and congruent tasks primarily highlights the lateral occipital cortex as the key region involved in distinguishing between the two, with a small percentage of voxels suggesting some involvement of the paracingulate gyrus. These regions were visible in FSLEYES during voxel thresholding, which, due to its conservative nature, only displays highly activated areas, particularly in COPE1 and COPE2. As a result, when the difference between the two tasks was calculated for COPE3, no regions were detected using voxel thresholding, as the subtle differences failed to meet the stringent criteria. In contrast, cluster thresholding, which accounts for spatially extended patterns of activity, was able to reveal these subtle activations, demonstrating that while voxel thresholding captures only the most robust signals, cluster thresholding

provides a more comprehensive view of the neural mechanisms underlying the tasks. This suggests that the lateral occipital cortex, and to a lesser extent the paracingulate gyrus, play a role in differentiating cognitive processing between incongruent and congruent tasks, although the differences are not pronounced enough to be fully captured by voxel-based methods.



fig.(25) COPE 3 activated regions

VI. Results

Region Of Interest

Based on prior studies of cognitive control, we focused our analysis on the paracingulate gyrus using a region of interest (ROI) approach. The mask for the paracingulate gyrus was defined using the MNI152 atlas. Z-statistics from the FEAT analysis were merged into a single file, and mean BOLD signals were extracted from the paracingulate gyrus mask for each subject across all contrasts of parameter estimate (COPEs). For each COPE, we obtained 26 values representing the average contrast estimate across voxels in the paracingulate gyrus. Positive values indicated greater BOLD activity during incongruent tasks compared to congruent tasks, while negative values suggested reduced activity or deactivation in the paracingulate gyrus during the task.

To assess the statistical significance of activation, a t-test was performed with the null hypothesis that the paracingulate gyrus was not activated during the task. The resulting p-value was 0.3412, exceeding the significance threshold of 0.05. Therefore, the null hypothesis could not be rejected, indicating no significant activation in this region during the task.

This result may be attributed to the size of the ROI, which included a substantial number of non-activated voxels. These non-activated voxels likely diluted the signal from the truly activated areas, thus impacting the overall statistical analysis.



fig.(26): Paracingulate Gyrus from MNI152 Atlas

Another method was to extract ROI with a smaller area than a whole region from an atlas. We start by revising past papers and search for related topics to shorten our search for the proper area to start with. Based on the study done in 2016 by Jahn et al who ran a similar research, it is found that there is a Conflict effect for a Stroop task - a distinct but related experimental design also intended to tap into cognitive control - with a peak t-statistic at MNI coordinates 0, 20, 40.

the dACC (MNI $-2, 30, 14$; $k = 788$; peak z-value = 5.17; $p < 0.001$, cluster-corrected; Fig. 4). In contrast, an analysis of conflict effects revealed a significant cluster more dorsally within the mPFC (MNI $0, 20, 44$; $k = 536$ voxels; peak z-value = 3.62; $p < 0.05$, cluster-corrected). Together with our previous analysis of

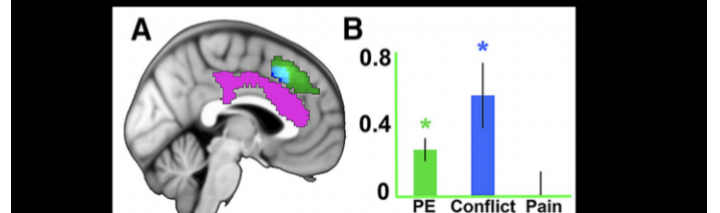


fig.(27): MNI Coordinates from 2016 study

We utilized FSLEYES to navigate from the MNI space to voxel space, using the 2mm MNI152_T1 image. Based on this, we determined that the required region in voxel space is at the coordinates (45, 73, 58). To create a new region of interest (ROI) around this point, a series of processing steps were applied. First, a file corresponding to the specified voxel coordinates was generated. The next step expanded this single point into a spherical ROI with a 5mm radius. Following this, the spherical ROI was binarized, assigning a value of 1 to the sphere and 0 to the surrounding voxels. Subsequently, we extracted the mean signal within the new ROI, similar to the process used for atlas-based extractions, yielding 26 values. A statistical t-test was then conducted on the new ROI, producing a p-value of 0.00020237. This value is below the significance threshold of 0.05, leading to the rejection of the null hypothesis and indicating that the mask was activated during the task. The same procedures were repeated for both COPE 1 and COPE 2, allowing us to compare the differences in activation between the atlas-defined gyrus and the newly created spherical ROI. These differences were then plotted to visualize the comparison.

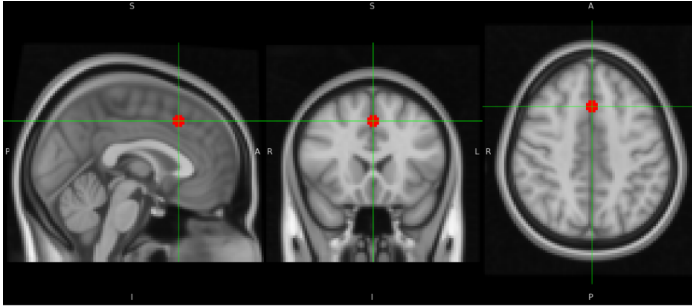


fig.(28): Sphere of radius 5 mm created at (45, 73, 58) in Voxel Coordinates

To visualize the mean values of x for each task, we generated plots using Matplotlib. The plots were enhanced by annotating significance levels: ** for p -values < 0.001 and * for p -values < 0.05 . These visualizations complement our statistical analysis, confirming the identified regions and the strength of the evidence supporting their activation.

	COPE1	COPE2	COPE3
PCG	0.45	0.35	0.101
Sphere	1.78	1.16	0.64

Table(0): Mean Values of x for each COPE

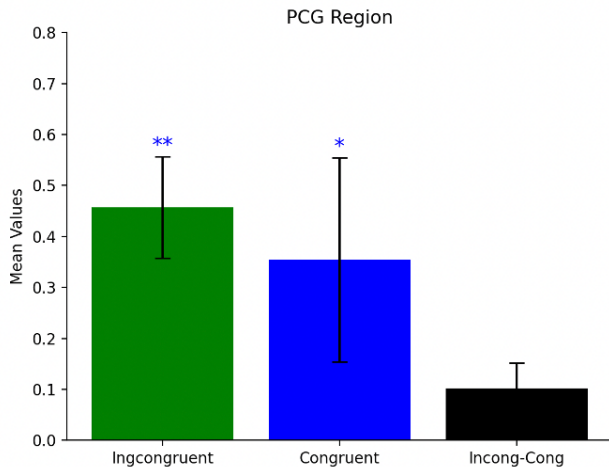


fig.(29): Paracingulate Region Mean Values of each task

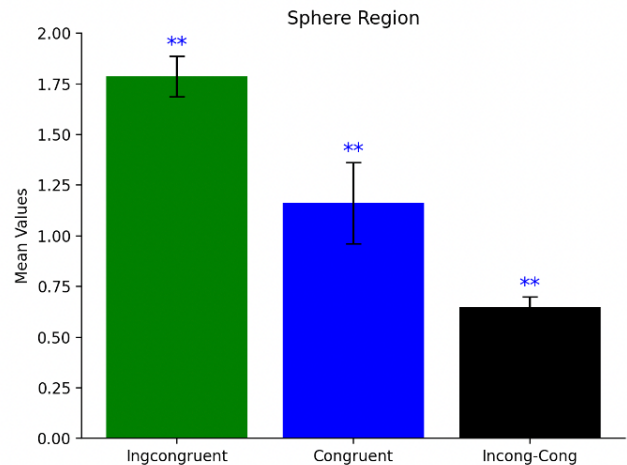


fig.(30): 5 mm Sphere Region Mean Values of each task

VII. CONCLUSIONS:

In this study, we analyzed regions of interest (ROIs) using both anatomical and spherical masks to investigate the neural mechanisms underlying cognitive control tasks. The anatomical ROI, based on prior research, did not yield significant results, suggesting that the selection of the ROI is critical to detecting relevant neural activity. However, the spherical ROI approach, focusing on maller region of the paracingulate gyrus, revealed significant activation during cognitive control tasks, particularly when contrasting incongruent and congruent conditions. This finding underscores the utility of applying a more flexible and tailored ROI approach, such as the spherical mask, to capture task-specific neural activity.

Our results highlight the paracingulate gyrus, along with other related brain regions, as key players in cognitive control, specifically in the monitoring of conflict and task regulation. These insights deepen our understanding of the neural networks involved in conflict resolution, decision-making, and cognitive flexibility, which are central to tasks that require higher-order executive function.

Future Work

Future research should aim to replicate these findings with more refined methods, such as smaller or more targeted ROIs, to mitigate the impact of non-activated voxels and improve the sensitivity of detecting brain activation. Further investigation could explore additional cognitive control tasks to assess whether the observed activation in the paracingulate gyrus generalizes across different experimental paradigms. Moreover, incorporating advanced techniques like machine learning for ROI definition or multivariate analysis could

help in identifying subtle and complex neural patterns that are difficult to capture with traditional approaches.

Additionally, expanding the analysis to include other brain regions implicated in cognitive control, such as the anterior cingulate cortex or the dorsolateral prefrontal cortex, would provide a more comprehensive view of the network involved in conflict monitoring and executive function. Combining these approaches with longitudinal studies could also offer insights into how these regions and their connectivity evolve over time, particularly in relation to aging, neurodevelopmental, and neurodegenerative disorders. Ultimately, refining the methods for ROI analysis and expanding our understanding of the paracingulate gyrus and its role in cognitive control could contribute to the development of targeted interventions for individuals with impaired cognitive function, including those with conditions such as ADHD, anxiety, or schizophrenia.

REFERENCES

- [1] “Introduction — Andy’s Brain Book 1.0 Documentation.” *Andysbrainbook.readthedocs.io*, andysbrainbook.readthedocs.io/en/latest/fMRI_Short_Course/fMRI_Intro.html.
- [2] Poldrack, Russell A. “Region of Interest Analysis for fMRI.” *Social Cognitive and Affective Neuroscience*, vol. 2, no. 1, Mar. 2007, pp. 67–70, academic.oup.com/scan/article/2/1/67/2362895.
- [3] Goebel, Rainer . “The General Linear Model (GLM).” *Www.brainvoyager.com*, www.brainvoyager.com/bv/doc/UsersGuide/StatisticalAnalysis/TheGeneralLinearModel.html. 2023,